Journal of Materials Chemistry A

ROYAL SOCIETY OF CHEMISTRY

PAPER

View Article Online
View Journal | View Issue

Cite this: J. Mater. Chem. A, 2023, 11, 20686

Understanding the electrochemical reaction mechanism to achieve excellent performance of the conversion-alloying Zn_2SnO_4 anode for Li-ion batteries†

Maciej Moździerz, [a] Zhenhe Feng,*[b] Agnieszka Brzoza-Kos,[a] Paweł Czaja,[c] Boyang Fu[a] and Konrad Świerczek *[ad]

Conversion-alloying-type compounds offer many new possibilities as anode materials for Li-ion cells, but also show some drawbacks related to their intrinsic characteristics. To overcome those limitations, the consecutive steps of electrochemical processes occurring in the selected Zn_2SnO_4 inverse spinel are studied in detail *i.e.* by *operando* X-ray diffraction, *ex situ* X-ray absorption spectroscopy, and transmission electron microscopy. Decomposition of the spinel phase upon the 1st lithiation proceeds with the precipitation of Li_2O and metallic particles, which further form LiZn and Li_xSn. A multicomponent matrix is created, which allows for reversible lithium storage. After dealloying upon the 1st delithiation, a Li_6ZnO_4/Li_4ZnO_3-type phase is formed in the conversion reaction, indicating reactivity between ZnO and Li_2O. Initially, α-Sn is likely precipitated, which is transformed into β-Sn during the 2nd cycle, indicating aggregation. Understanding the electrochemical reaction mechanism allowed identifying essential issues, important for the practical application of the Zn_2SnO_4 anode: too high reaction voltage *vs.* Li^+/Li with large hysteresis during the conversion reaction; metallic particle aggregation; large volume changes during deep (de-)alloying; mechanical problems on prolonged cycling. While the full-range capacity of the developed anodes reaches 920 mA h g^{-1} after 10 cycles at a current of 50 mA g^{-1} and over 460 mA h g^{-1} at 1000 mA g^{-1}, their operation range has to be limited in order to overcome the listed problems. This can be achieved by the controlled electrochemical prelithiation of Zn_2SnO_4 anodes before assembling full-cells. For the first time, excellent cycling stability is reached for micrometer-sized solid-state-synthesized Zn_2SnO_4, working in full Li-ion cells.

Received 28th April 2023
Accepted 31st August 2023

DOI: 10.1039/d3ta02549g

rsc.li/materials-a

1. Introduction

Due to constantly growing electrochemical performance demands, the ongoing development of next generation Li-ion batteries is focused mainly on an increase in gravimetric energy and power densities, with an obvious emphasis on the safety of their operation.[1–3] From the anode side, despite already reaching a close-to-theoretical capacity limit, the current market is still dominated by graphite anodes, with only some enhancement achieved by the implementation of a small amount (on the order of several wt%) of high-capacity silicon additives.[4–6] Among the many new groups of high-capacity anode materials being currently developed, the two most promising ones should be named, the so-called alloying and conversion materials.[7,8]

Alloying materials (*e.g.* metallic Si, Sn, Zn) offer extremely high theoretical gravimetric capacities, even up to 3578 mA h g^{-1} for Si-based anodes (assuming formation of $Li_{4.4}Si$), delivered through the formation of intermetallics with Li. The alloying process occurs usually at desirably low operating voltages (considering energy density of a full Li-ion cell), typically below 0.5 V.[7] Unfortunately, such anodes suffer from severe volume changes during the following (de-)lithiation cycles, leading to a poor cycling stability. While numerous approaches have been presented to overcome cyclability issues, with sophisticated synthesis methods used to obtain desired morphologies[7,9,10] or *e.g.* by formation of various composites,[11,12] as of today, only a small amount of Si could be introduced to commercial graphite anodes.[5]

[a]AGH University of Science and Technology, Faculty of Energy and Fuels, al. Mickiewicza 30, 30-059 Krakow, Poland. E-mail: xi@agh.edu.pl

[b]State Key Laboratory of Space Power-Sources Technology, Shanghai Institute of Space Power-Sources, No. 2965 Dongchuan Road, Shanghai 200245, China. E-mail: zhenhefeng2021@163.com

[c]Institute of Metallurgy and Materials Science, Polish Academy of Sciences, ul. Reymonta 25, 30-059 Krakow, Poland

[d]AGH Centre of Energy, AGH University of Science and Technology, ul. Czarnowiejska 36, 30-054 Krakow, Poland

† Electronic supplementary information (ESI) available. See DOI: https://doi.org/10.1039/d3ta02549g

The other groups of extensively studied alternative anodes are those working on the basis of the conversion reaction. Mainly, these are transition metal (TM) oxides (but also phosphides, sulfides, nitrides, hydrides, carbonates, and fluorides), for which a reversible formation of metallic TM nanoparticles and predominantly amorphous Li_2O can be observed on the course of the reaction with lithium.[3,8,13,14] While the achievable capacities for such compounds are lower compared to those for alloying materials (typically around 1000 mA h g^{-1}) and the operating voltage is higher (usually between 0.5 and 1.0 V,[8] resulting in a relatively lower energy density, but improved safety), the volume changes upon cycling are significantly lower.[13] Nevertheless, unresolved problems with a high initial irreversible Li consumption and an effect of voltage hysteresis, observed even for optimized compounds, hinder their application on a commercial scale.[15,16]

Searching for synergistic effects, a novel concept to combine both alloying and conversion reactions within a single material has been proposed, leading to the emergence of conversion-alloying materials (CAMs).[13,17] Similarly to pure conversion materials, CAMs can be oxides, but also compounds with various anions.[13] It can be anticipated for CAMs that products of the conversion reaction will help mitigate (at least to some degree) volume changes of the alloying reaction, while the specific energy density will be greatly increased as compared to pure conversion-based materials. Among the proposed CAMs, tin-containing inverse spinel oxides with a general formula of TM_2SnO_4 (TM = Zn, Co, Mn, but also Mg) have drawn particular attention.[17–22] This mainly stems from the possibility of obtaining highly lithiated Li–Sn intermetallics (*i.e.* $Li_{4.4}Sn$). Furthermore, as Zn also undergoes alloying with Li, the Zn_2SnO_4 spinel appears to be especially interesting regarding its reactivity with lithium in a voltage range of 0.01–3.0 V.[18,23,24] It is worth noting that while ZnO and SnO_2 can be used as anode materials by themselves,[13,18] the mixed single-phase Zn_2SnO_4 spinel has important advantages. Namely, the ratio between conversion and alloying reactions (originating from a 2 : 1 Zn^{2+} : Sn^{4+} ratio) is controlled and optimal, and, even more significantly, the mixing at the atomic scale is superior, yielding less particle aggregation (hence better long-term stability), different (more smooth) voltage profiles, and possibly the higher reversibility of electrochemical reactions.[25,26]

While there are no unambiguous results published, electrochemical reactions occurring in such a case are expected to occur as presented below.[24,27,28]

Initial conversion reaction:

$$Zn_2SnO_4 + 8Li^+ + 8e^- \rightarrow 2Zn + Sn + 4Li_2O \quad (1)$$

Reversible alloying reactions of Zn and Sn:

$$Zn + Li^+ + e^- \leftrightarrow LiZn \quad (2)$$

$$Sn + xLi^+ + xe^- \leftrightarrow Li_xSn, (0 < x \leq 4.4) \quad (3)$$

Reversible conversion reaction of Zn and Sn:

$$Sn + Zn + (1 + y)Li_2O \leftrightarrow SnO_y + ZnO + (2 + 2y)Li^+ + (2 + 2y)e^- \quad (1 \leq y \leq 2) \quad (4)$$

The extent and reversibility, as well as possible coexistence of different phases occurring for the above reactions are, among others, highly dependent on the applied voltage range, current density, and on the morphology of the active material. These issues are still not properly addressed yet, with discrepancies regarding the electrochemical reaction mechanisms present in the literature.[18,24,28–31] For example, the reported electrochemical performance of solid-state-synthesized Zn_2SnO_4 indicates the initial lithiation and delithiation capacities being relatively high, respectively 1150 mA h g^{-1} and 550 mA h g^{-1}.[18,32] However, due to the presence of substantial volumetric changes, the observed capacity fading was found to be very strong, yielding unacceptable performance only after several dozens of cycles.[18] Consequently, in most of the reports, solid-state synthesized Zn_2SnO_4 is not investigated, and, similarly to other candidate anode materials, literature studies on this CAM have been focused on developing different, usually very sophisticated nanostructural architectures, often associated with the usage of advanced synthesis techniques.[23,29,33–42] Indeed, a considerable improvement in the performance could be achieved, but to obtain satisfactory long-term cycling stability, expensive additives and different morphologies had to be used, *e.g.* graphene oxide,[23,29,33,35,38,41] nanotubes,[42] metal organic framework materials,[36] hollow boxes[37] and yolk(core)–shell design.[34,39,40] Such Zn_2SnO_4/C composites show significantly improved electrochemical performance compared with bare Zn_2SnO_4 electrodes. Specifically, Zn_2SnO_4 nanowires mixed with reduced graphene oxide display a discharge capacity of 983 mA h g^{-1} after 100 cycles at 55 mA g^{-1}.[41] Graphene-wrapped hollow Zn_2SnO_4 boxes were found to exhibit a capacity of 678 mA h g^{-1} after 45 cycles at 300 mA g^{-1} current.[37] A Zn_2SnO_4@V@PC composite, encapsulated within a porous carbon shell and forming a void structure delivers 438 mA h g^{-1} capacity after 600 cycles at 1000 mA g^{-1}.[34] Table S1† gathers recent reported characteristics of the developed Zn_2SnO_4-based anodes (with several reference data for other inverse spinels included). As can be summarized from the referenced papers, all of the so far proposed strategies to improve the performance of the Zn_2SnO_4 anode have been rather focused on the optimization at the material's morphology level, *i.e.* complex, composite-type nanostructures with carbonaceous materials have been developed. Chemical doping has not been considered yet, while selection of an appropriate binder and electrolyte additives is rarely discussed in this case. Regarding micrometer-sized Zn_2SnO_4, it is generally considered not suitable for application, because of its insufficient cycling stability.

Bearing in mind that often the elaborated and complex preparation techniques are hard to apply on a commercial scale, and in most cases are too expensive, we instead focus on overcoming the limitations and utilizing intrinsic advantages of the Zn_2SnO_4 material itself. Initially, the Li-storage and degradation mechanisms were thoroughly studied using *operando* X-ray diffraction (XRD), *ex situ* X-ray absorption spectroscopy (XAS),

and *ex situ* scanning electron microscopy (SEM) methods, giving a new insight into the actual reactions occurring for the Zn_2SnO_4 CAM and identifying the hindering steps, *i.e.* full conversion and deep (de-)alloying. Based on these results, we propose an electrochemical prelithiation of the anodes with a carefully selected final delithiation voltage. This allows controlling the range of the reactions, which is crucial for stable and high electrochemical performance. We also selected an optimal binder and liquid electrolyte additives, by which for the first time solid-state-synthesized Zn_2SnO_4 could be used to develop effectively working Li-ion anodes.

The conducted prelithiation and usage of styrene-butadiene rubber (SBR)/carboxymethyl cellulose (CMC) binder, as well as fluoroethylene carbonate (FEC) and vinylene carbonate (VC) electrolyte additives, together with Super P carbon, all ensure formation of the desired, rigid and stable anode matrix, buffering the unwanted volume changes, and having the necessary ionic and electronic charge migration networks. To study practical performance, the developed anodes were used with a commercial $LiNi_{1/3}Mn_{1/3}Co_{1/3}O_2$ (NMC111) cathode in Li-ion full-cells operating in a commercially useful voltage range of 2.25–4.2 V. The optimized cells show very good cyclability, with 79% capacity retention after 300 cycles at 0.5C, and a high capacity of 124 mA h g^{-1} (referring to the cathode active material's weight) at a high current of 1C. This is the best reported full-cell performance among the solid-state-synthesized conversion or conversion-alloying anodes reported so far. We believe that this work provides useful guidelines for practical implementation of solid-state-synthesized CAM-type anode materials in high-energy-density Li-ion batteries.

2. Experimental

2.1. Synthesis

Zn_2SnO_4 powder was prepared using a typical solid-state route. ZnO (Alfa Aesar, 99.99%) and SnO_2 (Alfa Aesar, 99.9%) starting chemicals were weighed in a stoichiometric ratio and mixed in isopropyl alcohol for 20 min using a high-energy ball mill Spex SamplePrep 8000M and zirconia milling balls. After drying, the obtained precursor was used to prepare pellets through uniaxial pressing under a pressure of 250 MPa, which were subsequently sintered in a tube furnace at 1200 °C for 20 h in air. Before further studies, the as-obtained sinters were manually ground for 30 min in an agate mortar.

2.2. Structural characterization

The crystal structure of the synthesized powder was characterized by the X-ray diffraction (XRD) method, using a Panalytical Empyrean diffractometer working in θ–θ Bragg–Brentano geometry with CuKα radiation and equipped with a PIXcel3D detector. The studies were conducted at room temperature (RT) in the 10–110 deg range, with one measurement lasting for *ca.* 50 min and with a resolution of 0.013 deg. The patterns were qualitatively analyzed using Panalytical HighScore software (ICDD PDF4+ 2021 database), while GSAS-II software[43] was used for the Rietveld refinement.

Raman spectra were measured at RT using a Thermo Scientific DXR3 Raman Microscope equipped with a 532 nm laser, 1800 grooves per mm grating, and a long working distance optical objective (50×). The spectra were collected in the 50–1800 cm^{-1} range with a resolution of 0.5 cm^{-1} at different spots on the sample's surface (to check the reproducibility of the measurements).

The morphology and chemical composition of the material were studied with scanning electron microscopy combined with energy dispersive X-ray spectroscopy (SEM/EDS) techniques using a Thermo Fisher Scientific Phenom XL and FEI Nova NanoSEM 200 apparatus. The experiments were conducted in secondary electron (SE) and backscattered electron (BSE) modes.

2.3. Preparation of Zn_2SnO_4 electrodes and electrochemical studies

Electrodes containing Zn_2SnO_4 were prepared using mixtures of the active material with Timcal Graphite & Carbon Super P and a respective binder. Two different types of binders were evaluated: poly(vinylidene fluoride) (PVDF, Kynar Arkema) and carboxymethyl cellulose (CMC, MTI) with styrene-butadiene rubber (SBR, 48% water solution, MTI). In the case of the PVDF binder, Zn_2SnO_4, carbon additive and the binder were mixed in a 70 : 20 : 10 weight ratio in *N*-methyl pyrrolidone (NMP) solvent using a high-speed Polytron PT 2500E homogenizer. For the CMC/SBR binder, initially, CMC was dissolved in water and mixed with the carbon additive and the active material overnight. Then, it was mixed with a water-based SBR solution to obtain a homogeneous slurry. The ratio of Zn_2SnO_4 : carbon : CMC : SBR was 70 : 20 : 5 : 5. In both cases, the obtained electrode slurries were coated onto 12 μm thick Cu foil using a doctor blade and then were vacuum-dried. The active material loading was controlled in a range of 2.1–2.3 mg cm^{-2} for PVDF and 2.4–2.6 mg cm^{-2} for CMC/SBR (*ca.* 10 μm thickness). Subsequently, 13 mm diameter discs were punched out, transferred into an Ar-filled glovebox (UNILab MBraun, Ar, H_2O <0.1 ppm, O_2 <0.1 ppm), and heated at 100 °C overnight. Inside the glovebox, CR2032 half-cells were assembled using the prepared electrodes, metallic Li foil (150 μm thick), Whatman (*ca.* 70 μm thickness) and Celgard 2400 (*ca.* 25 μm thickness) separators (16 mm diameter) and two different types of the electrolyte: unmodified 1 M $LiPF_6$ in 1 : 1 (v/v) ethylene carbonate (EC) : diethyl carbonate (DEC), and the same liquid electrolyte modified by the addition of 5 wt% of fluoroethylene carbonate (FEC) and 1 wt% of vinylene carbonate (VC).

All the electrochemical tests, including galvanostatic discharge/charge (GDC) and cyclic voltammetry (CV) techniques, were conducted using a Biologic VMP3 electrochemical workstation inside a thermostat set at 23 °C. The specific currents and capacities in the case of half-cells were calculated based on the weight of the active material. The voltage range in the studies was 0.01–2.5 V, while the current density was 200 mA g^{-1} for the cycling tests and 50–1000 mA g^{-1} in the rate capability measurements. In the CV experiments, the scan rate was 0.05, 0.1, 0.5, and 1.0 mV s^{-1}.

2.4. Preparation and optimization of the full-cells

To fabricate cathodes for the full-cells, the commercial $LiNi_{1/3}Mn_{1/3}Co_{1/3}O_2$ (NMC111) material was uniformly mixed with Timcal Graphite & Carbon Super P and PVDF binder, with a weight ratio of 82.5 : 7.5 : 10. The mixture was dispersed in the NMP solvent and coated onto 15 μm thick Al foil using the doctor blade method. The cast slurry was dried in a vacuum and finally punched into rounded NMC111 electrodes with 11 mm diameter. The active material loading was in the range of 8.4–8.9 mg cm^{-2} (*ca.* 120 μm thickness). The obtained discs were heated at 100 °C overnight.

2.4.1 Prelithiation of the Zn_2SnO_4 anodes. The CMC/SBR binder was selected for Zn_2SnO_4 anodes intended for full-cells. Their preparation was the same as that described in the previous section. The material loading was in the range of 2.5–3.2 mg cm^{-2}. Electrochemical prelithiation of the CAM anodes to a desired degree was used to compensate for the irreversible Li^+ consumption caused by the solid-electrolyte interphase (SEI) formation. To prepare prelithiated anodes, Zn_2SnO_4-based half-cells were (dis-)charged for 3 cycles at 100 mA g^{-1} with a final charge up to 0.4 V, 0.6 V, 0.8 V, 1.0 V or 2.5 V.

2.4.2 Full-cell assembly and electrochemical tests. As frequently reported, electrode alignment is one of the key parameters, which must be carefully controlled in the practical design of Li-ion full-cells. For example, a misaligned cell may show irreversible Li plating on a coin cell's bottom during the first charge process.[44,45] Particular attention was paid to align the 11 mm diameter cathodes and 13 mm diameter anodes correctly. The electrodes were assembled inside an Ar-filled glovebox into 2032 coin cells using the Whatman (*ca.* 70 μm thickness) and Celgard 2400 (*ca.* 25 μm thickness) separators (16 mm diameter) and 1 M $LiPF_6$ in 1 : 1 (v/v) EC : DEC electrolyte with the 5 wt% FEC and 1 wt% VC addition.

The electrochemical tests through the GDC technique were conducted using the same equipment as for the half-cells, at a constant temperature of 23 °C. The specific currents and capacities were calculated referring to the mass of cathode active material, assuming that 1C is equal to the practical capacity of NMC111 (150 mA h g^{-1}). For the cycling, the constant current–constant voltage (CC–CV) procedure was used. The cells were charged up to 4.2 V (CC step), and then the CV step was applied with the current limitation down to 0.01C. The discharge was down to 2.25 V (CC). After every full charge and discharge the cell was relaxed for 10 min.

2.5. *Operando* XRD and EIS, *ex situ* XAS, TEM, XRD and SEM studies

For the *operando* XRD measurements, a self-standing electrode was prepared by mixing the Zn_2SnO_4 active material, Timcal Graphite & Carbon Super P, CMC and SBR in a 70 : 15 : 7.5 : 7.5 weight ratio in water used as a solvent. The resulting slurry was coated onto a glass support using the doctor blade method and then was air-dried at room temperature (RT). The diameter of the obtained electrodes was 8 mm, and the active material loading was close to 4 mg cm^{-2}. Then, a custom-made electrochemical cell with a beryllium window, compatible with the Panalytical Empyrean diffractometer, was assembled in an Ar-filled glovebox using a Whatman separator, metallic Li foil, and 1 M $LiPF_6$ in 1 : 1 (v/v) EC : DEC electrolyte. The cell was galvanostatically (dis-)charged in a range of 0.01–2.5 V at a specific current of 50 mA g^{-1}. Each XRD measurement conducted in a 15–80 deg range lasted for 30 min, with a data resolution of 0.013 deg.

To study the charge transfer capability, the electrochemical impedance spectroscopy (EIS) measurements were performed at different (de-)lithiation stages during the 1st lithiation (discharge), 1st delithiation (charge), and 2nd lithiation (discharge). Here, this technique is referred to as *operando* EIS. A coin cell with the 1 M $LiPF_6$ in 1 : 1 (v/v) EC : DEC electrolyte and electrodes with the ratio of Zn_2SnO_4 : carbon : CMC : SBR set as 70 : 20 : 5 : 5 were cycled at a specific current of 50 mA g^{-1} in the voltage range of 0.01–2.5 V. The EIS measurements were conducted every 200 mA h g^{-1} during the 1st lithiation (including the measurement for the fresh cell) and every 100 mA h g^{-1} for the rest of the cycling, with 3 h of relaxation prior to each measurement. The spectra were collected in the 10^{-1} to 10^6 Hz frequency range with 10 mV disturbance amplitude. The analysis was performed using the distribution of relaxation times (DRT) approach with DRT-tools software.[46] The method allows separating contributions from different polarization processes, even for similar time constants, and therefore is extremely useful in studying (de-)lithiation mechanisms. Given the degree of complexity of the collected spectra, the analysis would be ambiguous and hard to perform by conventional fitting with equivalent circuits. Details about the derivation of the method can be found here.[46] The interpretation was based on previous reports on DRT used to study electrode materials for Li-ion cells, including our investigation of high-entropy CAM spinels.[25] Based on this, the regularization parameter was set to 10^{-3}. Before applying the DRT method, the spectra had been validated in terms of Kramers–Krönig relations using the Lin-KK Tool.[47]

For the *ex situ* SEM and X-ray absorption spectroscopy (XAS) measurements, the electrodes with the CMC/SBR binder and different electrolytes were (de-)lithiated for the selected number of cycles, relaxed for 8 h, disassembled inside the Ar-filled glovebox, and soaked in the DEC solvent overnight. To avoid oxidation, the samples were transferred to the respective apparatus inside Ar-filled sealed bags. The same procedure was used for *ex situ* SEM studies of different anodes from the full-cells. Soft XAS experiments were conducted at the end-station of the XAS beamline at the National Synchrotron Radiation Centre SOLARIS (Krakow, Poland). Zn $L_{3,2}$- and O K-edges were probed. The measurements were performed under high vacuum ($\leq 10^{-8}$ mbar) in the total electron yield mode (TEY, surface information up to *ca.* 10 nm) and in the partial fluorescence mode (PFY, bulk information up to *ca.* 100 nm).

For the *ex situ* XRD and *ex situ* transition electron microscopy (TEM) study, the samples were (de-)lithiated to a selected state. Because in this case the selected voltages were intermediate (neither full lithiation nor full delithiation), the voltage hold step was applied for 6 h. The cells were disassembled inside the Ar-filled glovebox and soaked in the DEC solvent overnight. For

the XRD measurements, a gas-tight holder compatible with the Panalytical Empyrean diffractometer was used to prevent air exposure. The tested 2θ range was the 15–50 deg range and the time was 1 h, with a data resolution of 0.013 deg. For the TEM measurements, ultrasonication in isopropyl alcohol and drop-casting on carbon-coated copper grids was applied. A Tecnai G2 F20 transmission electron microscope was used, operating at 200 kV accelerating voltage.

3. Results and discussion

3.1. Structure of the solid-state-synthesized Zn_2SnO_4

The synthesized Zn_2SnO_4 belongs to a group of 4–2 inverse spinels, with a general formula $[A^{2+}]^{tetrahedral}[A^{2+}B^{4+}]^{octahedral}O_4$.[17,48] The performed Rietveld refinement of the XRD data (Fig. 1a) confirms presence of the practically pure $Fd\bar{3}m$ phase with the unit cell parameter a = 8.6570(1) Å. The Raman spectroscopy data (Fig. 1b) further prove that Zn_2SnO_4 is the fully inverse spinel by showing the presence of only the expected five active modes for this structure (A_{1g}, E_g and three F_{2g}).[49] It is worth noting that there are no extra Raman modes visible on the spectrum, especially in the vicinity of the A_{1g} band, supporting that the Sn cations are occupying the octahedral positions exclusively.[50] Previous Mössbauer experiments[25] indicated the presence of Sn cations only at a +4 charge state, which further confirms the stoichiometry of the obtained material. At the microscale, the conducted SEM/EDS analysis (Fig. 1c) supports good homogeneity of the synthesized material, with no visible precipitations or inhomogeneous regions. The obtained micrometer-sized Zn_2SnO_4 powder has grains with a particle size well above 1 μm (see the results of DLS method studies, Fig. S1†).

3.2. Insight into the (de-)lithiation mechanism of Zn_2SnO_4 by *operando* XRD, EIS, *ex situ* XAS, and TEM

It is worth emphasizing that in this work the electrochemical working mechanisms were studied for the electrodes with a micrometer-sized Zn_2SnO_4 active material, without a complex nanoarchitecture, in order to minimize the complexity of the interpretation of the collected data.[51]

3.2.1 First lithiation of Zn_2SnO_4. Similarly to other CAMs,[17,19,52] Zn_2SnO_4 was reported to decompose on the first lithiation, which at the beginning proceeds as the conversion to Zn, Sn, and (amorphous) Li_2O (eqn (1)), and is accompanied by the SEI formation.[24,27] This irreversible step is clearly visible in the *operando* XRD data as a gradual decrease in intensity of the spinel phase-related peaks (Fig. 2a), as well as in *operando* EIS combined with DRT analysis as a significant change in the electrode's transport properties and a change in SEI resistance (ESI Note 1, Fig. S2†). It is also observed as a long plateau in a lithiation curve at *ca.* 0.47 V (Fig. 2d), with a corresponding specific current increase in the CV profile for voltages below *ca.* 0.5 V *vs.* Li^+/Li (Fig. 2e). Considering eqn (1), a theoretical capacity can be calculated to be 684 mA h g^{-1} for this step. With the decreasing intensity of Zn_2SnO_4-related XRD reflections, Zn peaks emerge and become distinguishable at lithiation levels above *ca.* 20% (*ca.* 3.2 moles of Li introduced per 1 mol of the initial material). Data for x = 44% (*ca.* 7.0 moles of the introduced Li) show a clearly visible, broad signal originating from metallic Zn particles (Fig. 2a). Notably, no reflections coming

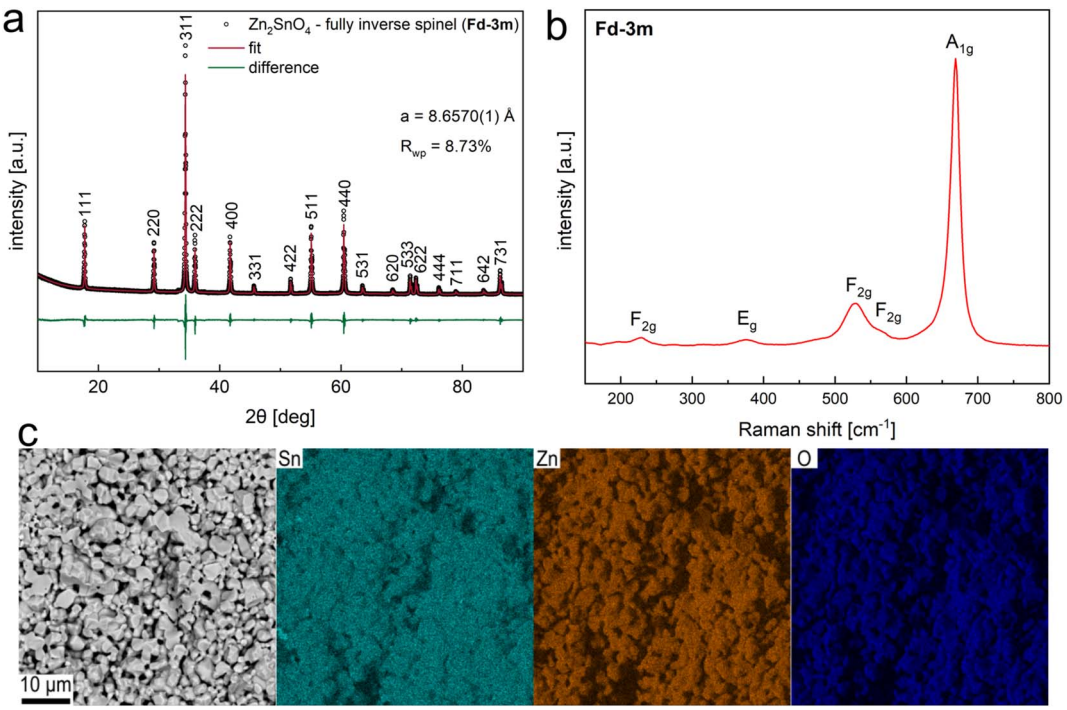

Fig. 1 Characterization of the solid-state-synthesized Zn_2SnO_4. (a) XRD data with Rietveld refinement, (b) Raman spectrum, and (c) SEM/EDS micrograph and elemental maps.

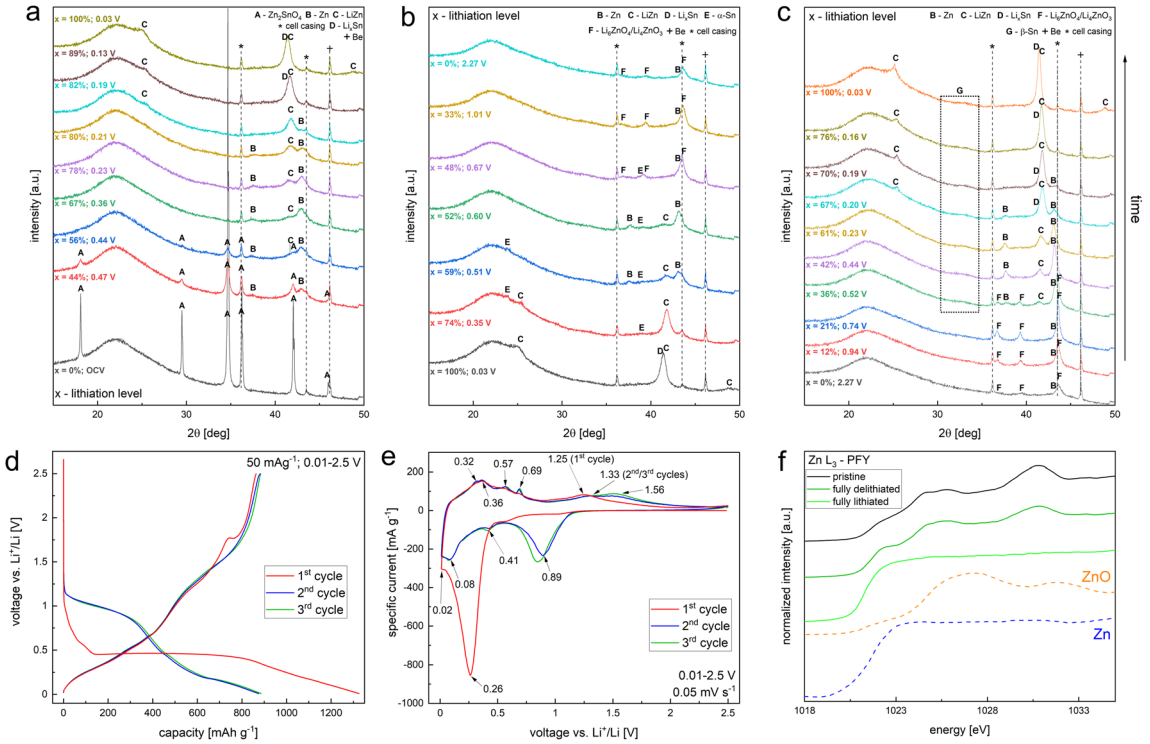

Fig. 2 Investigation of the (de-)lithiation mechanism for the Zn_2SnO_4 anode (CMC/SBR binder and $LiPF_6$ in EC:DEC electrolyte). The selected results of *operando* XRD studies for the 1st lithiation (a), 1st delithiation (b), and 2nd lithiation (c). The phases are marked with capital letters, while the signal from the *operando* cell and its Be window are marked with an asterisk and a plus sign, respectively (to identify this signal, comparison of the XRD patterns for the electrode layer outside and inside the cell was performed; the amorphous-like background corresponds to the used Whatman separator and carbon additive in the electrode). The percentage (x) for each diffractogram indicates the lithiation level based on the measured capacity. The presented voltage values were taken as the average during each measurement (due to unoptimized electrical contacts in the *operando* cell, they differ somewhat from the below reported electrochemical data). (d) Corresponding (de-)lithiation profiles recorded at the same current density and in the same voltage range. (e) Cyclic voltammetry study. The scan rate was 0.05 mV s^{-1} and the voltage range was 0.01–2.5 V. Average voltages of the maxima of the observed peaks are marked on the graph. (f) Zn L_3-edge XAS of the pristine, fully delithiated, and fully lithiated electrodes in half-cells in the partial fluorescence yield (PFY) mode, giving the bulk information, up to *ca.* 100 nm, together with reference data for ZnO and Zn (dashed lines).[55]

from metallic Sn could be identified at this stage, which is surprising, but matches the *ex situ* data published before for mechanochemically synthesized Zn_2SnO_4.[18] While the molar amount of Sn in the considered spinel is two times smaller than that of Zn, it is a heavier element. It can therefore be expected that the precipitated tin is rather in the form of well-dispersed nanoparticles, which are not observable in the *operando* XRD data. The behavior of Sn in the following cycles is found to be essential considering the electrochemical properties of the material, as documented in the next sections of the paper.

At $x = 56\%$ (*ca.* 9.1 moles of Li), a very weak and broad peak of the lithiated LiZn phase can be seen for the first time. This phase forms in the alloying process (eqn (2)), and according to the literature, it occurs at *ca.* 0.35 V.[24] In the reported case (Fig. 2a), the process rather proceeds continuously from *ca.* 0.44 V down to *ca.* 0.13 V. This corresponds to the sloping voltage decrease below the initial plateau (Fig. 2d), while for the CV data, it includes the maximum recorded specific current at *ca.* 0.26 V (Fig. 2e). As the alloying proceeds, for higher lithiation levels, the mentioned LiZn peak becomes much stronger, with more reflections visible originating from the discussed phase. The calculated contribution to the total capacity, for 2 moles of Zn per 1 mole of the Zn_2SnO_4 anode material, is 171 mA h g^{-1}.

A spinel-related signal is not detectable for $x = 67\%$ (*ca.* 10.9 moles of Li) and higher lithium contents in the electrode, and peaks of Zn are not visible for $x > 82\%$. Very fine, but noticeable phenomena take place at the final stages of the initial lithiation. There is a noticeable shift to the lower angles of a broad reflection present at about 42 deg (Fig. 2a), with a respective slight change of the lithiation curve slope in this range, at voltages below *ca.* 0.18 V (Fig. 2d). Considering the reported behavior of tin lithiation,[53,54] it can be overall concluded that (various) Li_xSn phases are being formed in this range (eqn (3)). Assuming the formation of highly lithiated $Li_{4.4}Sn$, the multi-step alloying should contribute up to a maximum capacity of 376 mA h g^{-1}.

In order to assess charge state changes of zinc and confirm the presence of the expected phases, XAS spectra (L_3-edge) were recorded and compared for the pristine and fully lithiated electrodes, as well as with the reference data (Fig. 2f). The initial charge is +2 for Zn in the spinel phase, while the signal after lithiation can be interpreted as Zn^0.[55] This is in agreement with the presence of LiZn intermetallics after reaction with lithium.

Summarizing the first lithiation, the sequence of the 1–3 reactions could be clearly observed in the *operando* XRD studies. The corresponding changes in the lithiation curve are also apparent; however, for the CV data, all the processes tend to blur. The observed total capacity is 1326 mA h g^{-1}, which is larger than the sum for the respective reactions 1–3 (1231 mA h g^{-1}). The difference can be inferred to originate from the following factors: SEI formation, which likely takes place throughout most of the lithiation process; a lack of the (evident) presence of highly lithiated $Li_{4.4}Sn$; a minor influence of the carbon additive in the composite electrode. One may also raise a question about the possible influence of the pseudo-capacitive nature on Li-storage by the present TM. The analysis of this phenomenon was based on CV data recorded at different scan rates and is presented in Fig. S3.†[56,57] As expected for the conversion reaction,[56] the character of the process is hybrid (b parameter equal to 0.87(5)), both pseudo-capacitive and diffusion controlled. Interestingly, while for the (de-)alloying reaction the Li-storage is still mixed, it is more diffusion controlled than in the case of conversion (smaller $b = 0.66(6)$). Therefore, the pseudo-capacitive storage in the case of the Zn_2SnO_4 material can also explain the excessive initial lithiation capacity.

3.2.2 Delithiation of the Li–Zn–Sn–O multicomponent matrix. The first delithiation of the formed Li_2O, LiZn, and Li_xSn matrix proceeds also through a series of processes occurring at different voltages (Fig. 2b). Initially, in a reverse manner in comparison to the lithiation, the broad peak visible at *ca.* 41.4 deg shifts to higher angles. This can be interpreted as dealloying of Li_xSn, as also confirmed by the emergence of metallic Sn reflections, clearly visible for x = 74–52%. Interestingly, the phase can be interpreted as α-Sn (cubic), which suggests precipitation of nanoparticles below a critical size of *ca.* 17 nm.[58] While α-Sn is semiconducting,[58,59] its influence on the charge transfer in the anode matrix in the first cycle should not be significant, as confirmed by the *operando* EIS data, in which the total polarization resistance was found not to increase in a range where this phase emerges (ESI Note 1, Fig. S2†). Simultaneously, the voltage (Fig. 2d) increases up to *ca.* 0.35 V on the delithiation curve, and there is a broad double feature visible in CV data, with local maxima at *ca.* 0.32 V and 0.36 V. All the results indicate multistep dealloying of Li_xSn, which is rather fully completed at this stage.[53,54,60]

In the next step, the signal of LiZn diminishes, while metallic Zn is already detectable at $x = 59\%$. Importantly, after the initial increase in intensity, Zn-related peaks remain observable practically in the whole delithiation range down to $x = 0$. This hints at not full reversibility of the following conversion process. Comparing *operando* XRD, delithiation curve, and CV data, it can be assumed that dealloying of LiZn proceeds up to *ca.* 0.9–1.0 V, above which this phase is not detectable anymore. It is also a multistep process.[61] Higher polarization of Zn dealloying, in comparison to Sn, should be noticed, indicating hampered kinetics.

The ZnO-related peak, which is detectable for $x \leq 33\%$ at *ca.* 36.9 deg emerges with two additional reflections, one at *ca.* 39.4 deg and another one (at the right side of the Zn signal) at 43.6 deg. This raises the question of whether really ZnO is created, as can be expected from eqn (4). Alternatively, these emerging peaks can be interpreted as originating from Li_6ZnO_4 (PDF 00-040-0202) and/or Li_4ZnO_3 phases (PDF 00-026-1210). This allows for proposing a different conversion step of the electrochemical reaction:

$$Zn + 4Li_2O \leftrightarrow Li_6ZnO_4 + 2Li^+ + 2e^- \quad (5)$$

Essentially, the above reaction also corresponds to the electrochemical activity of Li_2O as shown in eqn (4), but with only a limited amount of lithium extracted from the electrode. Also, there is no formation of a pure ZnO phase. Taking into account the Zn/Li_2O ratio in the anode matrix, which is 1 : 2, this also explains the presence of residual Zn upon full delithiation, as there is not enough Li_2O for the above reaction to proceed fully. Furthermore, it can be used to explain low initial coulombic efficiency, as lithium remains in the electrode not only in the SEI, but also being immobilized in the Li_6ZnO_4/Li_4ZnO_3 phases. Importantly, there are no clear detectable signals from SnO or SnO_2 phases, similarly to what was reported for the electrochemical reactivity of $Sn_{0.9}Fe_{0.1}O_2$ or similar cassiterite-structured oxides[53,54] and for Zn_2SnO_4 from *ex situ* XRD studies.[18] Consequently, the real extent of the tin conversion reaction at high voltages remains unresolved.

After full delithiation, the XAS signal of Zn (Fig. 2f) resembles the initial one (for the pristine sample), but is slightly shifted to lower energies, and less distinctive peaks (more smooth character of the spectrum) are present. This confirms that some amount of Zn^0 is still remaining in the material, matching the *operando* XRD data.

3.2.3 Lithiation of the multicomponent matrix. The second lithiation (Fig. 2c) begins with an unexpected phenomenon visible as an increase in intensity of the Li_6ZnO_4/Li_4ZnO_3-related peaks. This may be possibly explained by the changing ratio of those phases or by reactivity of the residual ZnO. At x = 36%, a signal from the metallic β-Sn (tetragonal) emerges. Since at higher voltages tin-related peaks could not be observed, initially Sn should remain oxidized in SnO_y-like amorphous phases. Looking at the differences in EIS spectra between the lithiation levels corresponding to the electrode containing Sn phase during the 1st delithiation (according to *operando* XRD data with α-Sn) and the 2nd lithiation (β-Sn, with the rest of the phases being similar), it can be noticed that the total polarization resistance is higher in the 1st cycle (ESI Note 1, Fig. S2†). Considering that Sn properties change from semiconducting to metallic between α and β allotropes, this supports the proposed polymorphic transition. Because β-Sn is formed in the 2nd lithiation, the precipitated particles must be larger, inferring aggregation.[58,59] Regarding Zn, between x = 21% and 42%, the content of Li_6ZnO_4/Li_4ZnO_3 phases significantly decreases, and at the same time, the intensity of the metallic Zn-related peaks at *ca.* 37.7 deg and at *ca.* 43.0 deg increases. The processes described above can be correlated with the broad CV peak during the 2nd cathodic scan between 1.15 V and 0.65 V (Fig. 2e) and the sloping voltage plateau in the same voltage range (Fig. 2d). Then, above the lithiation level of 36%, peaks from the

LiZn phase start to grow, with a simultaneous decrease of the metallic Zn reflections, for lithiation levels higher than 42%. The crystallites of the lithiated Li_xSn phases start to slowly grow above $x = 67\%$, with an abrupt increase in the main peak intensity below 0.16 V. These observations are in good agreement with the CV data (Fig. 2e), where the alloying of Zn occurs at *ca.* 0.41 V, while the formation of Li_xSn phases takes place at lower voltages (broad peak centered at *ca.* 0.09 V). This is also visible in the 2nd lithiation profile (Fig. 2d) as two different slopes, one around 0.5 V and the second starting at *ca.* 0.17 V.

To further corroborate the presence of the phases assigned in the *operando* XRD study, a sample was selected and investigated *via ex situ* TEM (Fig. 3, S4 and Table S2†). The phase composition of the selected sample corresponded to the 2nd lithiation stage during the *operando* XRD experiment, characterized by the lithiation level and a voltage of $x = 36\%$ and 0.52 V (Fig. 2c). This was confirmed by *ex situ* XRD and comparison with the *operando* XRD pattern, with both the results matching well (Fig. S5†). According to XRD, the phase composition is as follows: β-Sn; LiZn; Zn; Li_6ZnO_4/Li_4ZnO_3. The presence of all the expected phases was confirmed by selected area electron diffraction (SAED, Fig. 3a, b and Table S2†). Additionally, diffuse rings from partially amorphous Li_2O (not visible in the XRD) can be observed. This phase is expected to form during the conversion reaction and be present at the investigated lithiation level. The β-Sn nanoparticles, giving a weak signal in the XRD patterns (Fig. 2c), were clearly detected *via* high-resolution (HR) TEM, with an image of a representative particle with the corresponding fast Fourier transform (FTT) and inverse FTT shown in Fig. 3c–e. Importantly, the Li_6ZnO_4/Li_4ZnO_3-type phase could be observed in the SAED as well as HR-TEM mode (Fig. 3b and S4†), proving the proposed new stage of the conversion reaction (eqn (5)). Also, an attempt was made to detect the α-Sn particles with *ex situ* TEM for the sample taken after the first delithiation ($x = 48\%$), but the experiment was unsuccessful. It is likely that those metastable, very small nanoparticles (presumably below 17 nm (ref. 58)), transform during the sample preparation stage and/or interact with the high-energy electron beam during the measurement. Summarizing, it seems like the α-Sn phase can only be detected in the *operando*-type experiments.

Overall, while it can be stated that most of the electrochemical processes described above occur in a reversible manner, as evidenced by the similarly looking diffractograms at the end of the first and second lithiation, two main hindering effects, affecting practical application of the Zn_2SnO_4 anode, can be named. At the highest voltages, the Zn conversion reaction through Li_6ZnO_4/Li_4ZnO_3 phases exhibits high polarization, which is proven by a significant increase in charge transfer resistance during the 1st delithiation when these

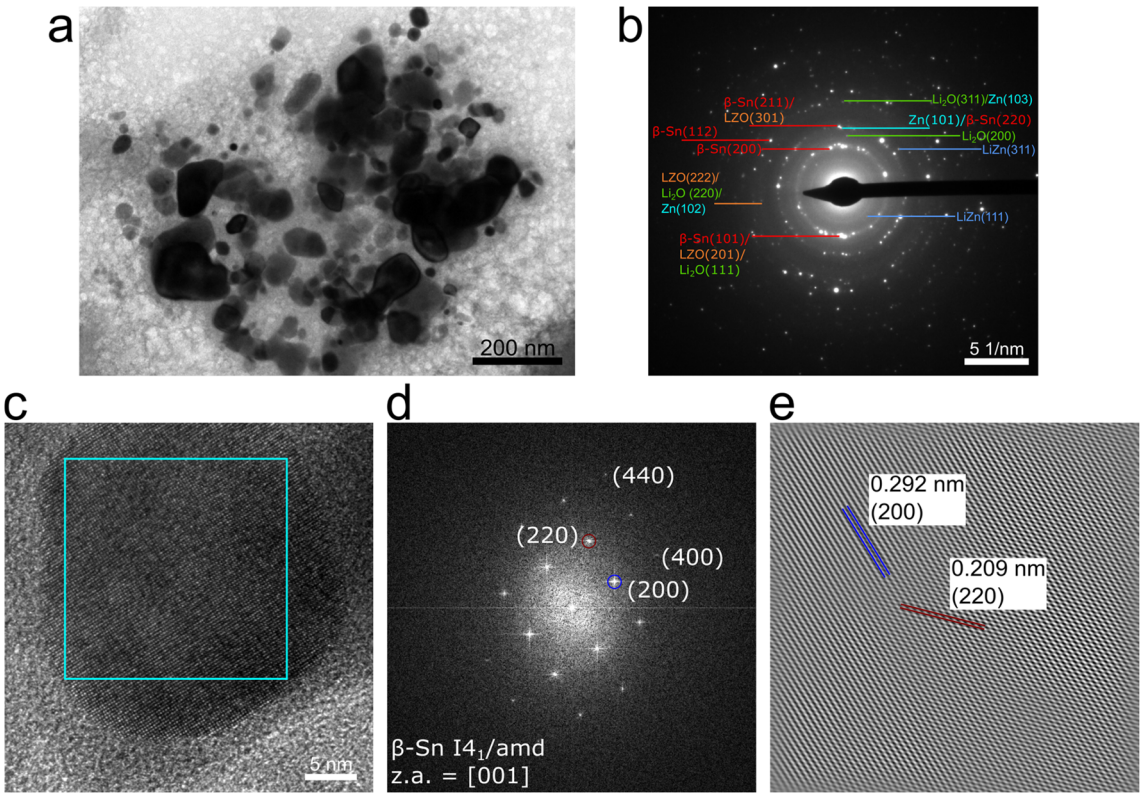

Fig. 3 *Ex situ* TEM characterization of the selected sample during 2nd lithiation. The sample corresponds to the XRD pattern at $x = 36\%$ (0.52 V) in Fig. 2c. (a) Bright-field TEM image with (b) the corresponding SAED pattern. The measured *d*-spacing values together with the phase assignment and PDF database numbers are presented in Table S2.† Due to overlapping of rings/spots in the measured pattern, some phases are marked collectively for clarity. The LZO abbreviation refers to the Li_6ZnO_4/Li_4ZnO_3 phase. (c) High-resolution (HR) TEM image of a single nanoparticle with (d) the fast Fourier transform (FTT) indexed as the tetragonal β-Sn phase. (e) Inverse FTT for the selected spots marked with circles.

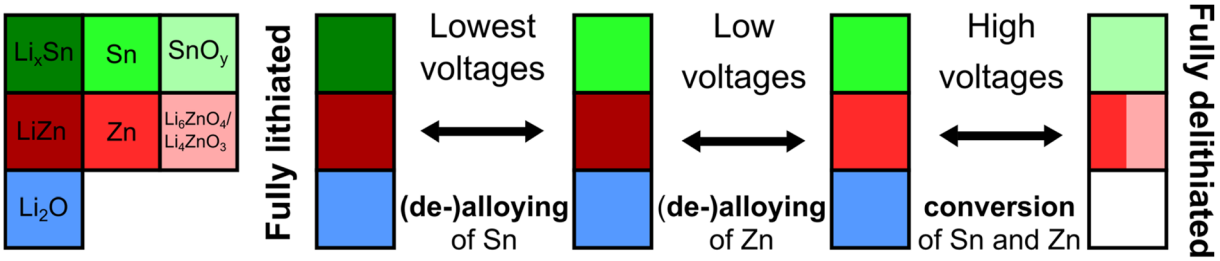

Scheme 1 Idealized diagram of the reversible electrochemical (de-)lithiation reaction mechanism for the Zn_2SnO_4 anode material.

phases are formed (ESI Note 1, Fig. S2†). On the other hand, at the lowest voltages, there is an unwanted aggregation of Sn and, to some extent, Zn nanoparticles (visible as the much narrower and more intense peaks related to Li_xSn and LiZn phases and the presence of the β-Sn phase, as compared with the 1st cycle). From this point of view, as well as taking into account huge volume changes during the formation of the highly lithiated Li_xSn phases,[62–64] *i.e.* leading to the SEI instability issues (increased SEI resistance based on EIS measured at the 2nd full lithiation, ESI Note 1, Fig. S2†), the optimal operating voltage range for the Zn_2SnO_4 anode should lie in the intermediate region, avoiding the highest voltages (full conversion reaction) and the lowest voltages (deep alloying reaction). The proposed electrochemical reaction mechanism is presented in the form of a (simplified) diagram in Scheme 1. It shows the reversible (de-)alloying of Sn at the lowest voltages, (de-)alloying of Zn at low voltages, and conversion of both Sn and Zn at higher voltages. Not shown, the initial irreversible lithiation reaction can be summarized as a sum of eqn (1)–(3).

3.3. Means of improvement of the electrochemical performance of Zn_2SnO_4 anodes

A proper selection of a binder and electrolyte additives is crucial for improving electrochemical performance of Zn_2SnO_4 anodes, especially regarding cycling stability. As presented in Fig. 4a and b, as well as in Fig. S6a and b,† replacement of the (more common) PVDF binder with CMC/SBR results in a significantly improved discharge capacity in the initial cycles. For both electrodes with the CMS/SBR binder (*i.e.* with or without FEC and VC additives), a characteristic behavior of an initial capacity decrease followed by an increase was observed. This is a well-known effect, typical for anode materials based on the conversion reaction mechanism, interpreted as originating from particle activation processes[56,65] and the so-called quasi-reversible formation of the SEI layer.[55] Superiority of the CMC/SBR binder over PVDF has also been previously reported for other CAMs[66,67] and generally for anode materials undergoing large volume changes during operation, as it allows for stronger binding with an active material and is more stable mechanically, remaining well-attached to a current collector during cycling.[68,69] Moreover, compared to PVDF, homogeneously distributed CMC provides a more efficient network of carbon, active material and binder, results in a lowered charge transfer resistance,[67] and influences the SEI composition, enhancing its stability.[70] CMC is often mixed with SBR, usually in the 1 : 1 proportion,[69,70] giving the composite electrode more desired flexibility and further improving the binding force.[68]

A question can also be raised, however, about the actual role of the electrolyte additives in the improved performance. As can be seen in Fig. 4b, and also in Fig. 4c, substantial enhancement of the cyclability could be achieved with FEC and VC addition to the electrolyte, with the capacity remaining above 640 mA h g^{-1} after 100 cycles, as well as largely improved behavior at high current densities. FEC addition results in the formation of a more stable SEI,[71,72] homogenously distributed over the active material's particles, and suppresses the degradation of $LiPF_6$.[72] Recently, it has been proposed that when FEC is combined with VC, products of their decomposition (highly cross-linked poly(ethylene oxide) polymers) prevent the further reduction of solvents, can easily accommodate the repeated expansion and contraction, and result in a better ionic conductivity of the SEI compared with purely EC-based electrolytes.[73] Here we studied the influence of these additives by analyzing the CV data for the first cycle (Fig. S7a†), as well as XAS data for the O K-edge (Fig. S7b and c†) for the electrodes. It is evident that the current peak corresponding to the SEI formation (Fig. S7a†) is at lower voltages for both the electrodes with the CMC/SBR binder. Additionally, it is further decreased when the FEC:VC-containing electrolyte is used, resulting in a more kinetically stable film.[70,74] Regarding XAS data (Fig. S7b and c†), the surface signal (TEY) for the electrode lithiated and delithiated in the electrolyte with additives shows fewer changes (in comparison to the unmodified electrolyte), especially at *ca.* 535 eV, which further supports the formation of a more stable SEI. At the same time, the bulk signal (PFY, up to *ca.* 100 nm) for the electrode cycled in the modified electrolyte is more similar to the surface one, in both lithiated and delithiated states, indicating that the formed SEI is thicker. For the unmodified EC:DEC electrolyte changes between lithiated and delithiated states are more prominent, confirming a less stable SEI layer.

Interestingly, for all the considered anodes, an activation-like phenomenon (*i.e.* a sudden voltage increase and then decrease) occurs upon the first delithiation (Fig. 4a, S6a and S6b†). Taking into account the XRD *operando* data (Fig. 2a–c) and a sequence of the electrochemical processes, it appears that it is related to the zinc and/or tin oxidation during conversion, although the nature of the subsequent polarization decrease remains unknown (no structural changes in this range could be identified). Notably, the magnitude of the phenomenon is smaller for both CMC/SBR anodes.

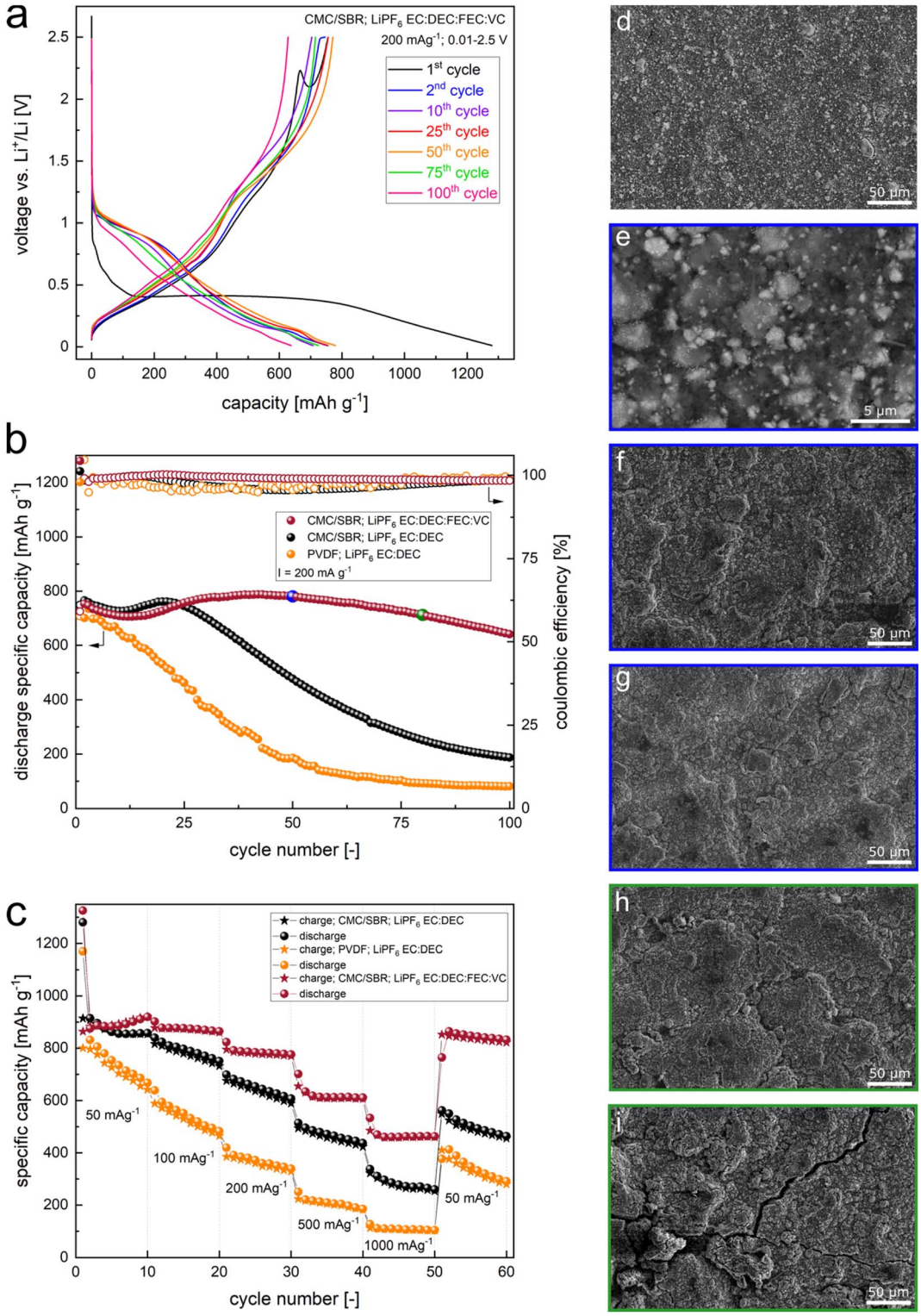

Fig. 4 Electrochemical performance of Zn_2SnO_4 in half-cells. (a) GDC curves for the cycling stability tests for 100 cycles at a specific current of 200 mA g^{-1} in the voltage range of 0.01–2.5 V for the cell with the CMC/SBR binder and $LiPF_6$ in EC:DEC:FEC:VC electrolyte. (b) Collective plot of discharge capacity as a function of cycle number comparing cells with different binder/electrolyte setups: PVDF/$LiPF_6$ in EC:DEC; CMC/SBR/$LiPF_6$ in EC:DEC; CMC/SBR/$LiPF_6$ in EC:DEC:FEC:VC. The corresponding GDC curves are presented in Fig. S6a and b.† The bolded blue point marked on the graph refers to the *ex situ* SEM data after 50 cycles presented in (e–g), while the bolded green point refers to the *ex situ* SEM data after 80 in (h and i). (c) Rate capability tests in the voltage range of 0.01–2.5 V for different binder/electrolyte setups at various specific currents, as described on the graph. The GDC curves for the best setup are presented in Fig. S6c.† (d–i) *Ex situ* SEM for electrodes with the CMC/SBR binder cycled at a current of 200 mA g^{-1} in half-cells with $LiPF_6$ EC:DEC:FEC:VC electrolyte: (d) pristine, observed in SE mode, (e) fully lithiated after 50 cycles, observed in BSE mode, (f) fully lithiated after 50 cycles, observed in SE mode, (g) fully delithiated after 50 cycles, observed in SE mode, (h) fully lithiated after 80 cycles, observed in SE mode, and (i) fully delithiated after 80 cycles, observed in SE mode.

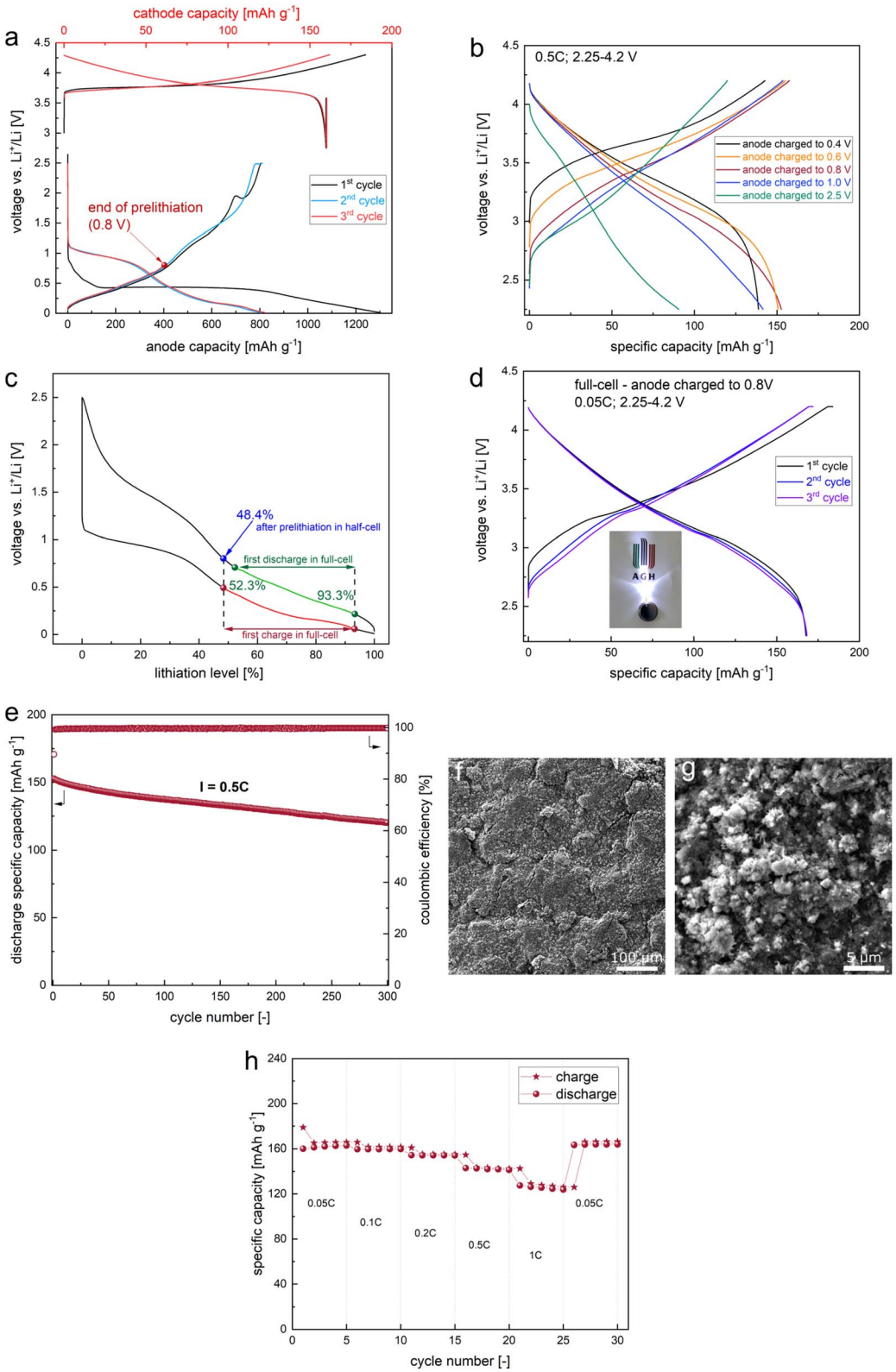

Fig. 5 Electrochemical performance of Zn_2SnO_4 in full-cells. (a) GDC curves for the Zn_2SnO_4 anode (0.01–2.5 V, 100 mA g^{-1}) and NMC111 cathode (2.75–4.3 V, 0.05C) measured in half-cells for three cycles with the marked prelithiation voltage for the anode. (b) 1st cycle GDC curves for the full-cells with the anodes prelithiated to 0.4, 0.6, 0.8, 1.0, and 2.5 V in the voltage range of 2.25–4.2 V at a current of 0.5C. (c) Operation range in the full-cell during the 1st charge and discharge for the Zn_2SnO_4 anode prelithiated to 0.8 V, demonstrated on the voltage profile measured for the half-cell with Zn_2SnO_4. The calculations were based on the known capacities of the full-cell as well as half-cells with Zn_2SnO_4 and NMC111 active materials. (d) GDC curves for the three initial cycles for the full-cell with the anode prelithiated to 0.8 V, cycled in the voltage range of 2.25–4.2 V at a current of 0.05C; the inset displays a 6 mW LED lit up by a full-cell. (e) Long-term stability tests for the full-cell in the

The optimized Zn_2SnO_4 anode with the CMC/SBR binder, as well as with FEC and VC electrolyte additives shows a capacity of 920 mA h g^{-1} after 10 cycles at a low current density of 50 mA g^{-1} (Fig. 4c). Its capacity stabilizes at 464 mA h g^{-1} at a high current of 1000 mA g^{-1}. When going back to the low current, the capacity is almost fully recovered, yielding a capacity retention value of 99% (comparing discharge capacities after the 52nd and 2nd cycles). Also, a cycling test at a specific current of 500 mA g^{-1} revealed relatively high values of capacity exceeding 500 mA h g^{-1} during the initial 125 cycles. However, a capacity degradation, similar to that presented in Fig. 4c, could be observed in the following cycles. Concerning the previously reported data (Table S1†), the registered rate capability outperforms most of the results presented for bare Zn_2SnO_4 electrodes, even for the nanosized material and electrodes with the PVDF[42,75] or CMC binder.[34,66] Noteworthily, such good stability has never been achieved for spinel-type CAMs, even for more advanced synthesis methods and resulting microstructures, unless the material was coated/combined with carbonaceous materials (*e.g.* reduced graphene oxide, nanowires, *etc.*, please see Table S1† for a detailed comparison).[22,26,30–39,60,69,76]

More insight into the morphology changes for the best performing Zn_2SnO_4 anode was provided by SEM studies, as presented in Fig. 4d–i. It is evident that after 50 cycles the electrode's morphology becomes coarser in comparison to the pristine one, but still no cracks could be seen. Nevertheless, the larger magnification presented in Fig. 4e reveals an ongoing aggregation of the metallic nanoparticles (for comparison with the high magnification image of the not-agglomerated pristine electrode see Fig. S8†), being in agreement with *operando* XRD data. However, a substantial change could be observed after 80 cycles, with obvious cracks visible in the delithiated state (Fig. 4i), but surprisingly, the micrograph of the lithiated anode (Fig. 4h) shows a microstructure with much smaller, almost unnoticeable cracks. This indicates that most of the cracking occurs at high voltages and at deeper delithiation levels, suggesting that such a range should be excluded from the operational range. In fact, the improved stability of the Zn_2SnO_4 electrode could be obtained previously by cycling in the limited voltage range (up to 1.5 V) and therefore preventing full delithiation.[24]

Summarizing the above findings, as well as taking into account the mechanism of the electrochemical reaction, as studied in the previous subchapter, it is evident that achieving stable performance of the Zn_2SnO_4 anode must be related to the limitation of the high delithiation range (to avoid cracking and exclude large voltage hysteresis), and the deep lithiation degree should be excluded, due to the ongoing aggregation of metallic nanoparticles and large volume changes for highly lithiated intermetallics (increasing the total volume change between discharge and charge).

3.4. Development of high-energy-density Li-ion full-cells with the Zn_2SnO_4-based anode

For the tests in the Li-ion full-cells (CR2032), the designed Zn_2SnO_4 anode with the CMC/SBR binder was taken. A commercial NMC111 cathode was selected, and the used electrolyte had FEC and VC additions. Initially, the recorded stable specific capacities of about 800 mA h g^{-1} for Zn_2SnO_4 (0.01–2.5 V, 100 mA g^{-1}) and 160 mA h g^{-1} for NMC111 (2.75–4.3 V, 0.05C) electrodes were confirmed in the half-cells (Fig. 5a). As mentioned in the Experimental section, electrochemical prelithiation was applied to the Zn_2SnO_4 anodes, during which Li/Li^+/Zn_2SnO_4 half-cells were discharged (lithiation) down to 0.01 V and charged (delithiation) up to 2.5 V *vs.* Li/Li^+ for three cycles. During such processes the active material undergoes decomposition and the precipitated phases are reversibly lithiated, which enables the formation of a Li_2O matrix with a well-connected network of metallic particles. At the same time, the mechanical stability of the electrode is not an issue during initial cycles, while the problem of the still insufficient initial coulombic efficiency (ICE), which is *ca.* 59% for the used electrodes, can be mitigated. The final step of the prelithiation involved a charge up to a selected voltage from the 0.4–2.5 V range. According to Scheme 1, this corresponds to different phase compositions of the Zn_2SnO_4-based electrodes taken for preparation of the full-cells. In particular, it can be summarized as follows: the electrode prelithiated to 0.4 V: Sn, LiZn, and Li_2O; 0.6 V: Sn, LiZn/Zn, and Li_2O; 0.8 V: SnO_y, Zn, Li_6ZnO_4/Li_4ZnO_3, and Li_2O; 1.0 V: SnO_y, Zn, Li_6ZnO_4/Li_4ZnO_3, and Li_2O (more TM oxide phases); 2.5 V: SnO_y, Zn, and Li_6ZnO_4/Li_4ZnO_3 (even more TM oxides).

Regarding the practical, prolonged operation of the Zn_2SnO_4-based electrode, the findings from the mechanism study (Section 3.2) showed the necessity of exclusion of the unwanted high voltage range *vs.* Li^+/Li, while utilization of the lower voltage alloying process is desired, as it yields high energy density. The above mentioned (voltage) controlled prelithiation enabled for the first time a proper control of the operation range of the Zn_2SnO_4 electrode. This is clearly visible in the 1st cycle voltage profiles measured for the Li-ion full-cells with different anodes (Fig. 5b). While the cycling voltage range for all the full-cells was kept in the useful range between 2.25 V and 4.2 V, the registered profiles vary significantly depending on the prelithiation voltage. If the final prelithiation voltage was set at 2.5 V and 1.0 V, the 1st discharge specific capacities (Fig. 5b, calculated considering the cathode active material mass) are clearly lower than the available cathode capacity, making these cells anode limited. This corresponds to a situation in which a part of the anode's capacity lies at too high voltages *vs.* Li^+/Li, so it cannot be utilized (unless going to lower voltages, below 2.25 V). On the other hand, if the prelithiation voltage is too low (0.4 V), the anode is initially highly lithiated and all the available Li^+ from the cathode cannot be stored. In this case the cell is

2.25–4.2 V range at a current of 0.5C for 300 cycles. (f and g) *Ex situ* SEM analysis in SE mode after 300 cycles. (h) Rate capability tests at various specific currents in the voltage range of 2.25–4.2 V. All the presented specific capacities and currents for the full-cells were calculated considering the mass of cathode active material.

also anode limited. Since the goal in this work was to make the full-cells cathode limited and have high capacity (the configuration used in the commercial Li-ion batteries[77]), this could be achieved only for the cells with the anodes prelithiated to 0.6 V and 0.8 V. Of importance, we decided not to utilize the lower voltage range of the full-cells, as sometimes reported in the literature.[78–80] Looking at the long-term cycling stability (Fig. S9†), the 0.8 V prelithiation is superior to 0.6 V prelithiation. In this particular case, upon the first full-cell charge (anode lithiation), the anode changed its lithiation level from *ca.* 48.4% up to 93.3% (presented schematically in Fig. 5c). On the following discharge, the lithiation level was 41.0%. This reflects the utilization of almost exclusively the alloying part of the electrochemical processes (Scheme 1, Fig. 2), but without going to the lowest voltages *vs.* Li^+/Li, which, according to our previous discussion, should be avoided. For prelithiation voltages of 0.4 V and 0.6 V, the formation of highly lithiated intermetallics on too deep alloying resulted in worsened cycling stability. On the other hand, for prelithiation to 1.0 V the discharge capacity and average reaction voltage were lower, as the operation range is shifted toward greater utilization of the conversion process. As expected, the prelithiation to 2.5 V led to the worst electrochemical performance because the anode operates only in the conversion reaction regime (quite good cycling stability but very poor energy density, both due to the lack of an alloying-type reaction). Based on all these results, in the following section we provide detailed analysis only for the 0.8 V prelithiation voltage.

The recorded initial three (dis-)charge cycles at 0.05C for the full-cell are presented in Fig. 5d. Notably, only a small CV part of the charge can be seen after the initial CC charge. A specific capacity of about 168 mA h g^{-1} was achieved in the 3rd discharge cycle for this cell (at 23 °C), as calculated in relation to the weight of NMC111. Notably, the specific energy density for the cell was calculated to be 367 W h kg^{-1} (based on the total weight of the cathode and pristine anode active materials) in the first discharge. This value is higher than the energy density of the full-cells utilizing *e.g.* high-entropy oxide-based conversion anodes (*ca.* 240 W h kg^{-1})[81] and exceeds that of most CAM cell systems listed in Table S3.†

The recorded cycling performance for 300 cycles is displayed in Fig. 5e. Evidently, the cell shows very good cycling stability, with 120 mA h g^{-1} capacity (in relation to the cathode) remaining after 300 cycles, and with a capacity fade rate of only 0.26% per cycle. During the whole cycling process, the coulombic efficiency was stabilized at above 99.6%. To assess the contribution of the performance degradation from both electrodes, the full-cell was disassembled and the cathode was tested again in a new half-cell. It was found that the capacity fade after 300 cycles for the cathode was *ca.* 10 mA h g^{-1} (from *ca.* 159 mA h g^{-1} down to 149 mA h g^{-1}, as shown in Fig. S10†), indicating that the remaining contribution comes from the anode.

To further elaborate on the degradation mechanism, SEM observations of the Zn_2SnO_4 anode were conducted after 300 cycles (Fig. 5f). It is evident that no obvious cracks are present, contrary to the full range operation in the half-cell (Fig. 4i), proving the effectiveness of the proposed approach in this paper. Higher magnification reveals some morphological changes after prolonged cycling, but with only a limited aggregation of the nanoparticles (Fig. 5g). Finally, Fig. 5h depicts the rate performance of the considered full-cell over current densities ranging from 0.05C to 1C. The cell delivers 123.8 mA h g^{-1} after 5 cycles at a 1C rate, which is still 76% of that at a 0.05C rate. Moreover, it can recover a high capacity of 163.9 mA h g^{-1} again after 5 cycles when the current density is back to 0.05C, indicating very good rate performance.

4. Conclusions

Summarizing the paper, it can be stated that effectively working conversion-alloying anodes can be developed on the basis of the solid-state-synthesized Zn_2SnO_4 spinel. It is possible to overcome the intrinsic limitations of the material, which could be successfully identified through comprehensive investigations on the nature of the (de-)lithiation mechanism (*operando* XRD and EIS, *ex situ* XAS, SEM and TEM), by the selection of an appropriate binder and liquid electrolyte additives, as well as uncovering the causes of performance degradation. The new findings allowed for a careful choice of the prelithiation voltage (0.8 V), which enables usage of the desired range of the electrochemical reaction at the almost exclusively (de-)alloying reaction part but without going to the lowest voltages *vs.* Li^+/Li. This is the key parameter for obtaining good full-cell performance from the Zn_2SnO_4 anode. High-energy-density Li-ion full-cells (CR2032) were manufactured and tested, with the specific energy density above 360 W h kg^{-1} (first discharge, calculated in relation to the total weight of the pristine anode and cathode materials), and with almost 80% capacity retention after 300 cycles. All this emphasizes the fact that Li-ion batteries with CAM-type anodes can and should be optimized, not only by the modification of the active material itself but also by considering numerous different parameters.

Conflicts of interest

There are no conflicts to declare.

Acknowledgements

This research was supported by the National Science Centre, Poland, (NCN) on the basis of the decision number UMO-2019/35/O/ST5/01560. Sections regarding full-cells of this research project were supported by the AGH Excellence Initiative – Research University program (IDUB AGH, grant no. 501.696.7996, Action 4, ID 6354). This publication was developed under the provision of the Polish Ministry of Education and Science project: "support for research and development with the use of research infrastructure of the National Synchrotron Radiation Centre SOLARIS" under contract nr 1/SOL/2021/2. We acknowledge the SOLARIS Centre for access to the XAS beamline, where the measurements were performed. Raman spectroscopy measurements were conducted on the apparatus purchased with financial support from the AGH

Excellence Initiative – Research University program (IDUB AGH, Action 8). Zhenhe Feng gratefully acknowledges financial support from the China Scholarship Council. (CSC No. 202004980033).

References

1 S. Chu, Y. Cui and N. Liu, *Nat. Mater.*, 2016, **16**, 16–22.
2 Y. Sun, N. Liu and Y. Cui, *Nat. Energy*, 2016, **1**, 16071.
3 N. Mahmood, T. Tang and Y. Hou, *Adv. Energy Mater.*, 2016, **6**, 1600374.
4 G. G. Eshetu, H. Zhang, X. Judez, H. Adenusi, M. Armand, S. Passerini and E. Figgemeier, *Nat. Commun.*, 2021, **12**, 1–14.
5 H. F. Andersen, C. E. L. Foss, J. Voje, R. Tronstad, T. Mokkelbost, P. E. Vullum, A. Ulvestad, M. Kirkengen and J. P. Mæhlen, *Sci. Rep.*, 2019, **9**, 1–9.
6 P. Li, H. Kim, S. T. Myung and Y. K. Sun, *Energy Storage Mater.*, 2021, **35**, 550–576.
7 M. N. Obrovac and V. L. Chevrier, *Chem. Rev.*, 2014, **114**, 11444–11502.
8 K. Cao, T. Jin, L. Yang and L. Jiao, *Mater. Chem. Front.*, 2017, **1**, 2213–2242.
9 S. Kilian, K. McCarthy, K. Stokes, T. E. Adegoke, M. Conroy, I. S. Amiinu, H. Geaney, T. Kennedy and K. M. Ryan, *Small*, 2021, **17**, 1–8.
10 A. Varzi, L. Mattarozzi, S. Cattarin, P. Guerriero and S. Passerini, *Adv. Energy Mater.*, 2018, **8**, 1701706.
11 R. Mo, X. Tan, F. Li, R. Tao, J. Xu, D. Kong, Z. Wang, B. Xu, X. Wang, C. Wang, J. Li, Y. Peng and Y. Lu, *Nat. Commun.*, 2020, **11**, 1–11.
12 S. Fang, L. Shen, S. Li, G. T. Kim, D. Bresser, H. Zhang, X. Zhang, J. Maier and S. Passerini, *ACS Nano*, 2019, **13**, 9511–9519.
13 D. Bresser, S. Passerini and B. Scrosati, *Energy Environ. Sci.*, 2016, **9**, 3348–3367.
14 J. Cabana, L. Monconduit, D. Larcher and M. R. Palacín, *Adv. Mater.*, 2010, **22**, 170–192.
15 D. Puthusseri, M. Wahid and S. Ogale, *ACS Omega*, 2018, **3**, 4591–4601.
16 Y. Lu, L. Yu and X. W. Lou, *Chem*, 2018, **4**, 972–996.
17 M. V. Reddy, G. V. Subba Rao and B. V. R. Chowdari, *Chem. Rev.*, 2013, **113**, 5364–5457.
18 S. M. Becker, M. Scheuermann, V. Sepelák, A. Eichhöfer, D. Chen, R. Mönig, A. S. Ulrich, H. Hahn and S. Indris, *Phys. Chem. Chem. Phys.*, 2011, **13**, 19624–19631.
19 R. Alcántara, G. F. Ortiz, P. Lavela and J. L. Tirado, *Electrochem. Commun.*, 2006, **8**, 731–736.
20 S. Lei, K. Tang, C. Chen, Y. Jin and L. Zhou, *Mater. Res. Bull.*, 2009, **44**, 393–397.
21 T. Xiao, Y. Tang, Z. Jia and S. Feng, *Electrochim. Acta*, 2009, **54**, 2396–2401.
22 J. Zhang, J. Liang, Y. Zhu, D. Wei, L. Fan and Y. Qian, *J. Mater. Chem. A*, 2014, **2**, 2728–2734.
23 B. Y. Wang, H. Y. Wang, Y. L. Ma, X. H. Zhao, W. Qi and Q. C. Jiang, *J. Power Sources*, 2015, **281**, 341–349.
24 C. T. Cherian, M. Zheng, M. V. Reddy, B. V. R. Chowdari and C. H. Sow, *ACS Appl. Mater. Interfaces*, 2013, **5**, 6054–6060.
25 M. Moździerz, K. Świerczek, J. Dąbrowa, M. Gajewska, A. Hanc, Z. Feng, J. Cieślak, M. Kądziołka-Gaweł, J. Płotek, M. Marzec and A. Kulka, *ACS Appl. Mater. Interfaces*, 2022, **14**, 42057–42070.
26 H. Kim, D. H. Seo, H. Kim, I. Park, J. Hong, K. Y. Park and K. Kang, *Chem. Mater.*, 2012, **24**, 720–725.
27 X. Hou, Q. Cheng, Y. Bai and W. F. Zhang, *Solid State Ionics*, 2010, **181**, 631–634.
28 N. Kim, J. H. Shim, W. Jae, J. Song and J. Kim, *J. Alloys Compd.*, 2019, **786**, 346–355.
29 W. Song, J. Xie, W. Hu, S. Liu, G. Cao, T. Zhu and X. Zhao, *J. Power Sources*, 2013, **229**, 6–11.
30 X. J. Zhu, L. M. Geng, F. Q. Zhang, Y. X. Liu and L. B. Cheng, *J. Power Sources*, 2009, **189**, 828–831.
31 A. Rong, X. P. Gao, G. R. Li, T. Y. Yan, H. Y. Zhu, J. Q. Qu and D. Y. Song, *J. Phys. Chem. B*, 2006, **110**, 14754–14760.
32 F. Belliard, P. A. Connor and J. T. S. Irvine, *Solid State Ionics*, 2000, **135**, 163–167.
33 L. Qin, S. Liang, X. Tan and A. Pan, *J. Alloys Compd.*, 2017, **692**, 124–130.
34 J. Song, X. Lu, Q. Tian, L. Cui, J. Chen and Z. Sui, *J. Alloys Compd.*, 2022, **910**, 164924.
35 W. Song, J. Xie, S. Liu, G. Cao, T. Zhu and X. Zhao, *J. Mater. Res.*, 2012, **27**, 3096–3102.
36 X. Zheng, Y. Li, Y. Xu, Z. Hong and M. Wei, *CrystEngComm*, 2012, **6**, 2112–2116.
37 Y. Zhao, Y. Huang, Q. Wang, K. Wang, M. Zong, L. Wang, W. Zhang and X. Sun, *RSC Adv.*, 2013, **3**, 14480–14485.
38 Y. Zhao, Y. Huang, X. Sun, H. Huang, K. Wang, M. Zong and Q. Wang, *Electrochim. Acta*, 2014, **120**, 128–132.
39 Y. J. Hong and Y. C. Kang, *Nanoscale*, 2014, **7**, 701–707.
40 T. Jiang, X. Tian, H. Gu, H. Zhu and Y. Zhou, *J. Alloys Compd.*, 2015, **639**, 239–243.
41 Y. R. Lim, C. S. Jung, H. S. Im, K. Park, J. Park, W. Il Cho and E. H. Cha, *J. Mater. Chem. A*, 2016, **4**, 10691–10699.
42 L. Qin, S. Liang, A. Pan and X. Tan, *Mater. Lett.*, 2016, **164**, 44–47.
43 B. H. Toby and R. B. Von Dreele, *J. Appl. Crystallogr.*, 2013, **46**, 544–549.
44 V. Murray, D. S. Hall and J. R. Dahn, *J. Electrochem. Soc.*, 2019, **166**, A329–A333.
45 N. Kim, S. Byun, D. Jin, C. B. Dzakpasu, S. H. Park, H. Lee, S. Hong and Y. M. Lee, *J. Electrochem. Soc.*, 2022, **169**, 023502.
46 T. H. Wan, M. Saccoccio, C. Chen and F. Ciucci, *Electrochim. Acta*, 2015, **184**, 483–499.
47 M. Schönleber, D. Klotz and E. Ivers-Tiffée, *Electrochim. Acta*, 2014, **131**, 20–27.
48 K. E. Sickafus, J. M. Wills and N. W. Grimes, *J. Am. Ceram. Soc.*, 1999, **82**, 3279–3292.
49 Q. Ma, S. Wu and Y. Fan, *Ceram. Int.*, 2014, **40**, 1073–1080.
50 V. Šepelák, S. M. Becker, I. Bergmann, S. Indris, M. Scheuermann, A. Feldhoff, C. Kübel, M. Bruns, N. Stürzl, A. S. Ulrich, M. Ghafari, H. Hahn, C. P. Grey, K. D. Becker and P. Heitjans, *J. Mater. Chem.*, 2012, **22**, 3117–3126.
51 A. R. Akbashev, *ACS Catal.*, 2022, **12**, 4296–4301.

52 L. Fang, N. Bohlawane, W. Sun, H. Pan, B. B. Xu, M. Yan and Y. Jiang, *Small*, 2021, **17**, 2101137.
53 Y. Ma, Y. Ma, G. Giuli, T. Diemant, R. J. Behm, D. Geiger, U. Kaiser, U. Ulissi, S. Passerini and D. Bresser, *Sustainable Energy Fuels*, 2018, **2**, 2601–2608.
54 J. Asenbauer, A. L. Wirsching, M. Lang, S. Indris, T. Eisenmann, A. Mullaliu, A. Birrozzi, A. Hoefling, D. Geiger, U. Kaiser, R. Schuster and D. Bresser, *Adv. Sustainable Syst.*, 2022, **6**, 2200102.
55 T. Eisenmann, J. Asenbauer, S. J. Rezvani, T. Diemant, R. J. Behm, D. Geiger, U. Kaiser, S. Passerini and D. Bresser, *Small Methods*, 2021, **5**, 21–25.
56 D. Wang, S. Jiang, C. Duan, J. Mao, Y. Dong, K. Dong, Z. Wang, S. Luo, Y. Liu and X. Qi, *J. Alloys Compd.*, 2020, **844**, 156158.
57 T. He, X. Kang, F. Wang, J. Zhang, T. Zhang and F. Ran, *Mater. Sci. Eng., R*, 2023, **154**, 100737.
58 N. Oehl, L. Hardenberg, M. Knipper, J. Kolny-Olesiak, J. Parisi and T. Plaggenborg, *CrystEngComm*, 2015, **17**, 3695–3700.
59 A. U. Haq, S. Askari, A. McLister, S. Rawlinson, J. Davis, S. Chakrabarti, V. Svrcek, P. Maguire, P. Papakonstantinou and D. Mariotti, *Nat. Commun.*, 2019, **10**, 1–8.
60 J. H. Shin and J. Y. Song, *Nano Convergence*, 2016, **3**, 3–9.
61 J. J. A. Kreissl, J. Petit, R. Oppermann, P. Cop, T. Gerber, M. Joos, M. Abert, J. Tübke, K. Miyazaki, T. Abe and D. Schröder, *ACS Appl. Mater. Interfaces*, 2021, **13**, 35625–35638.
62 Y. Wang, J. Y. Lee and H. C. Zeng, *Chem. Mater.*, 2005, **17**, 3899–3903.
63 P. Zhang, Z. Ma, Y. Wang, Y. Zou, W. Lei, Y. Pan and C. Lu, *RSC Adv.*, 2015, **5**, 36022–36029.
64 J. Wang, F. Fan, Y. Liu, K. L. Jungjohann, S. W. Lee, S. X. Mao, X. Liu and T. Zhu, *J. Electrochem. Soc.*, 2014, **161**, F3019–F3024.
65 A. Sarkar, L. Velasco, D. Wang, Q. Wang, G. Talasila, L. de Biasi, C. Kübel, T. Brezesinski, S. S. Bhattacharya, H. Hahn and B. Breitung, *Nat. Commun.*, 2018, **9**, 3400.
66 R. Zhang, Y. He and L. Xu, *J. Mater. Chem. A*, 2014, **2**, 17979–17985.
67 D. Bresser, E. Paillard, R. Kloepsch, S. Krueger, M. Fiedler, R. Schmitz, D. Baither, M. Winter and S. Passerini, *Adv. Energy Mater.*, 2013, **3**, 513–523.
68 A. Cholewinski, P. Si, M. Uceda and M. Pope, *Polymers*, 2021, **13**, 631.
69 R. Wang, L. Feng, W. Yang, Y. Zhang, Y. Zhang, W. Bai, B. Liu and W. Zhang, *Nanoscale Res. Lett.*, 2017, **12**, 575.
70 L. El Ouatani, R. Dedryvère, J. B. Ledeuil, C. Siret, P. Biensan, J. Desbrières and D. Gonbeau, *J. Power Sources*, 2009, **189**, 72–80.
71 X. Chen, X. Li, D. Mei, J. Feng, M. Y. Hu and J. Hu, *ChemSusChem*, 2014, **7**, 549–554.
72 C. Xu, F. Lindgren, B. Philippe, M. Gorgoi, F. Bjorefors, K. Edstrom and T. Gustafsson, *Chem. Mater.*, 2015, **27**, 2591–2599.
73 T. Liu, S. Paul, P. C. M. M. Magusin, R. S. Weatherup, E. Jo and C. P. Grey, *J. Am. Chem. Soc.*, 2018, **140**, 9854–9867.
74 E. Peled and S. Menkin, *J. Electrochem. Soc.*, 2017, **164**, A1703–A1719.
75 H. Fan, Z. Liu, J. Yang, C. Wei, J. Zhang and W. Zheng, *RSC Adv.*, 2014, **4**, 49806–49810.
76 S. Yuvaraj, W. J. Lee, C. W. Lee and R. K. Selvan, *RSC Adv.*, 2015, **5**, 67210–67219.
77 X. Wu, K. Song, X. Zhang, N. Hu, L. Li, W. Li, L. Zhang and H. Zhang, *Front. Energy Res.*, 2019, **7**, 1–17.
78 J. Asenbauer, A. Varzi, S. Passerini and D. Bresser, *J. Power Sources*, 2020, **473**, 228583.
79 A. Varzi, D. Bresser, J. Von Zamory, F. Müller and S. Passerini, *Adv. Energy Mater.*, 2014, **4**, 1400054.
80 J. Asenbauer, J. R. Binder, F. Mueller, M. Kuenzel, D. Geiger, U. Kaiser, S. Passerini and D. Bresser, *ChemSusChem*, 2020, **13**, 3504–3513.
81 Q. Wang, A. Sarkar, Z. Li, Y. Lu, L. Velasco, S. S. Bhattacharya, T. Brezesinski, H. Hahn and B. Breitung, *Electrochem. Commun.*, 2019, **100**, 121–125.

